Vertical dispersion of an aircraft wake: Aerosol-lidar analysis of entrainment and detrainment in the vortex regime

Ralf Sussmann

Fraunhofer-Institut fur Atmosphärische Umweltforschung, IFU, Garmisch-Partenkirchen, Germany

Abstract. Vertical dispersion of contrails in the vortex regime is investigated by focusing on the role of entrainment and detrainment of exhaust with respect to the pair of trailing vortices. A ground-based backscatter-depolarization lidar with an integrated CCD camera provides information on optical and geometrical parameters of the contrail in the time span between 5.7 and 50.3 s behind a B747-400 aircraft. This is combined with coincident airborne in situ measurements of turbulence and the vertical profiles of temperature and wind speed in a case study. The two wingtip vortices, separated by 47 m, are descending with an increasing speed (2.5–3.1 m/s for 10.8–47.8 s behind aircraft) in the weakly non-stably-stratified atmosphere. The turbulent vertical dissipation rate on the day of the study above southern Germany is a factor of 1000 higher than found typically above oceans at cruising altitude. At 4.2 s behind the aircraft, a diffuse secondary wake starts to evolve above the two wingtip vortices. After ≈ 50 s the secondary wake encloses a cross-sectional area (4410 m^2) comparable to that of the primary wake (4620 m^2) and a relative ice surface area of 1:5. The observed early onset of the secondary wake is conjectured to be due to turbulent detrainment of fluid out of the primary wake which can be enhanced by detrainment due to baroclinic forces later in the vortex regime evolution. By exclusion of other mechanisms of secondary wake formation, detrainment of fluid from the primary wake is concluded to be the precondition for secondary wake formation. Detrainment due to baroclinic forces, shear or turbulence is, in general, unlikely to be absent for typical atmospheric conditions. It is suggested that the ambient humidity level may determine when a secondary wake is visible above a vortex pair and when it is not.

1. Introduction

The physical and chemical state of the atmosphere near the tropopause is influenced by the emissions of cruising aircraft [*Schumann*, 1994]. Chemical evolution and microphysics (ice growth) inside an aircraft wake depend strongly on the concentration of species and temperature, i.e., on dynamic parameters. The dynamic evolution of an aircraft wake can be classified into three subsequent stages commonly referred to as the jet, the vortex, and the dispersion regimes [*Hoshizaki et al.*, 1975]. In the jet regime the exhaust is found within the individual jets behind each engine. After a few seconds behind aircraft, the jets are entrained into the pair of trailing vortices that roll up behind the wing tips of aircraft. Within the vortex regime the exhaust is assumed to be strongly captured by the vortex pair until the vortices become unstable and break up (≈ 2 min behind aircraft). This is the beginning of the dispersion regime, in which further dispersion is determined primarily by the vertical shear of the horizontal wind speed and on ambient turbulence.

Several investigations have been performed in the dispersion regime, for example, an estimate of diffusion parameters of aircraft exhaust plumes from nitric oxide and turbulence measurements [*Schumann et al.*, 1995], or the characterization of cross-sectional growth in the late wake, experimentally [*Freudenthaler et al.*, 1995], and numerically [*Gierens, 1996; Dürbeck and Gerz*, 1996]. It was found that for timescales

larger than minutes the plume spreads mainly horizontally by shear and turbulence in the ambient air that is stably stratified, usually with large bulk Richardson numbers [*Schumann et al.*, 1995].

Most of the vertical dispersion, however, is assumed to be due to the initial vertical descent induced by the trailing vortex pair during the vortex phase. The dilution of exhaust is significantly affected by being entrained and isolated from the ambient air by the counterrotating pair of trailing vortices. Thus to understand vertical dispersion, it is necessary to know the mechanisms of entrainment of exhaust into the trailing vortices, possible detrainment of fluid out of the vortex system during the descent, and finally, the instability processes at the end of the life span of the vortices. Various investigations of the development of trailing vortices have been performed by the aircraft community since the 1970s. Turbulence-induced Crow instabilities and vortex bursting were described [*Crow*, 1970; *Chevalier*, 1973; *Spalart and Wray*, 1996], and the influence of stratification and shear [*Robins and Delisi*, 1989; *Schilling et al.*, 1996], or stratification and ambient turbulence [*Greene*, 1986, *Sarpkaya and Daly*, 1987] on vortex descent and life span, have been investigated, mainly theoretically. Recent work focuses on wake prediction [*Greene*, 1986] for Air Traffic Control being able to deal with the wake hazard problem near airports [*Spalart*, 1997]. However, in no case were all relevant meteorological influences (stratification, shear, and turbulence) on dynamical vortex evolution and destruction treated together in the same model. Recent modeling investigated the wake-exhaust mixing [*Quackenbush et al.*, 1996] relevant for environmental research, as outlined above. Most recent
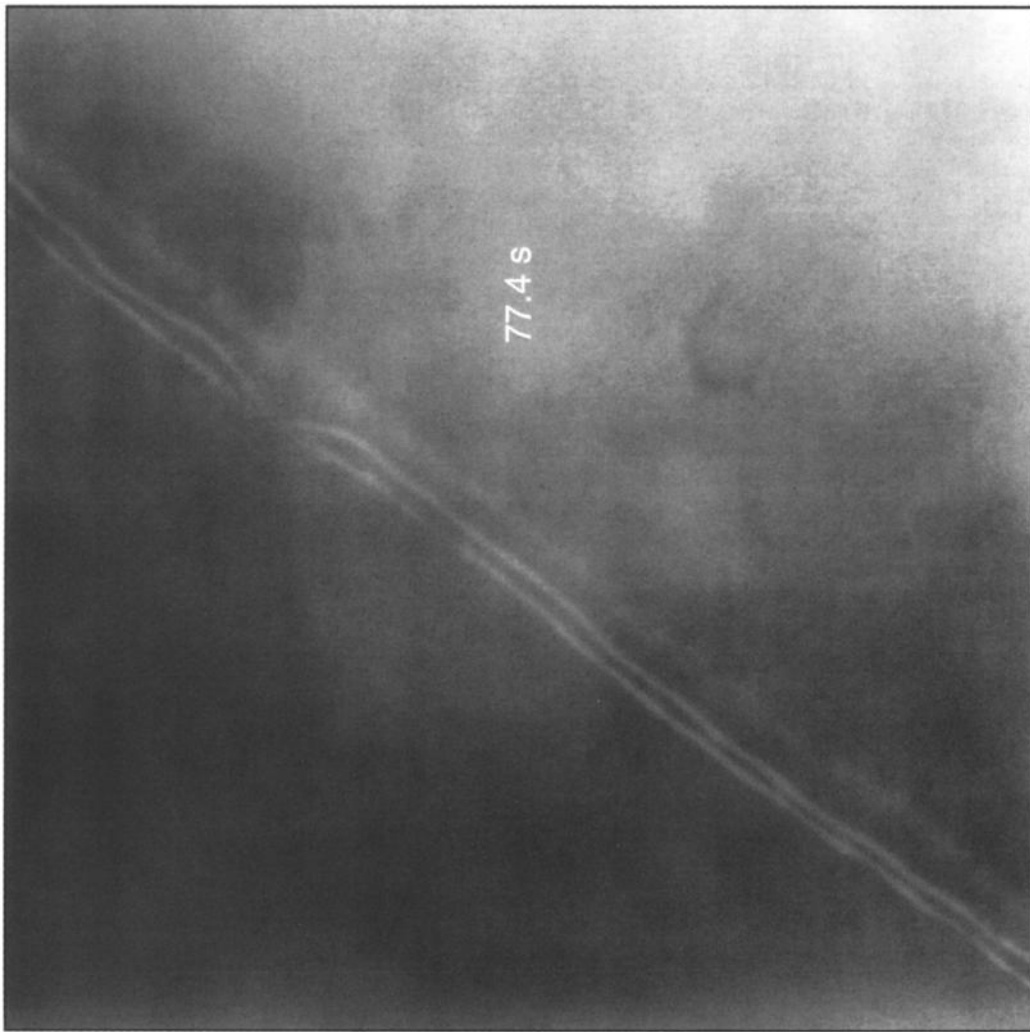
Figure 1. CCD image of the contrail of the B-747-400 aircraft investigated in this work (77.4 s behind aircraft). Note the "secondary-wake phenomenon," i.e., a diffuse third plume above the pair of wingtip vortices.

achievements in modeling allow the simulation of the total dynamic life span of a wake, including the starting roll-up process of the vortices, and exhaust entrainment and detrainment up to the end of the vortex regime [*Gerz and Ehret*, 1996, 1997; *Gerz and Kärcher*, 1996; *Lewellen and Lewellen*, 1996].

In this work we investigate experimentally the dynamic behavior of the wake of a B747 aircraft in the vortex regime. This is the first experimental investigation of a diffuse "secondary wake" above the "primary wake" (Figure 1). (Throughout this paper "primary wake" means both the system of the two counterrotating wingtip vortices behind aircraft and the ice contained inside; "secondary wake" is the less ordered flow and ice above the primary wake.) This is interesting because the secondary wake and the vortex pair undergo different chemical and microphysical histories. The resulting entrainment rates for the primary emissions determine the rate and extent of their mixing with the ambient air, and this is important for the atmospheric chemistry because chemical processes evolve nonlinearly [*Danilin et al.*, 1992; *Miake-Lye et al.*, 1993; *Karol and Ozolin*, 1994]. Secondary wake formation affects the microphysics since it leads to different conditions for the growth of ice particles compared to the primary wake. This strongly im-

pacts the total ice mass in a contrail [*Sussmann and Gierens*, this issue].

The goal of this paper is twofold. First, we address the fact that there is a significant lack of experimental data on the exhaust wake evolution in the vortex regime, i.e., vortex descent and cross-sectional evolution. We will present a new experimental data set, including the characterization of the cross-sectional evolution of the dynamic system of a vortex pair and its secondary wake, an analysis of all meteorological parameters relevant for the dynamical evolution and all relevant aircraft parameters. This shall give modelers the opportunity to check simulations of aircraft exhaust wake evolution during the vortex phase. The second goal of this paper is using our experimental data to give new input to the current debate on different physical mechanisms that possibly contribute to secondary-wake formation. Discussions were hitherto based on theoretical considerations only [*Gerz and Ehret*, 1996; *Schilling et al.*, 1996; *Spalart*, 1997; *Gierens and Ström*, 1998]. For this we perform an evaluation of the various different mechanisms given in the literature that possibly contribute to the secondary-wake phenomenon. We discuss our observations of typical dynamic features that have not been predicted by theoretical

modeling. Our research presented in this paper is limited to four-turbofan aircraft.

2. Measurement Techniques

The analysis reported here is based on coincident measurements by the IFU ground-based lidar and airborne in situ devices carried by the research aircraft FALCON (Deutsches Zentrum für Luft- und Raumfahrt (DLR)). We are now using a combined lidar and CCD camera approach to investigate the specific scattering properties of the ice particles within contrails [*Sussmann*, 1997] and to combine lidar information with larger-scale observations by CCD camera and satellite imaging [*Sussmann et al.*, 1996]. The IFU bistatic backscatter-depolarization lidar [*Freudenthaler et al.*, 1995] consists of a Nd–Yag laser (Quanta-Ray GCR-4-10, 550 mJ pulse energy at 532 nm, ≤0.5 mrad beam divergence), a 52 cm diameter Cassegrain telescope with Chopper, two photomultipliers (THORN EMI 9218A with range gate switch) for perpendicular polarization orientations, four channels of simultaneous analog sampling (Kontron W&W700, 10 bit/50 MHz transient digitizer), and it is combined with a CCD camera (Sony XC-77CE, focal length f = 12.5–75 mm, field of view (fov) = 40°, 756 × 581 pixel, video processor (AEG), frame grabber (Matrox)) oriented parallel to the laser axis. The lidar is operated in the single-shot mode with a 10 Hz repetition rate and a range resolution of 3 m. Integration of the whole system on a two-axis scanning mount with a pointing accuracy that exceeds the laser beam divergence allows for tracking and cross-sectional measurements of contrails. For this the horizontal drift speed of the contrail (typically 20 m/s) is preestimated from lidar sounding (altitude) and video-image analysis (angular velocity). On the basis of these data the lidar-CCD-camera mount is computer controlled to track the drifting contrail. The cross section of a contrail is then scanned relative to this drifting coordinate system using typically 20 subsequent scanning directions (10 laser pulses each). For each scanning direction, one CCD image is recorded. The accurate wind vector at contrail altitude is postprocessed from the location of a significant contrail feature during the video series. An image of backscatter signal versus contrail cross section is obtained by graphical interpolation between the lidar profiles of the individual measurement directions.

Meteorological parameters at the location of the contrail investigated by the ground-based lidar are derived from data measured onboard the FALCON research aircraft of the DLR. We use in situ data of the temperature sensor as well as data of the wind-speed and turbulence-measuring system. The latter records the wind velocity components for the east-west (u), north-south (v), and vertical (w) directions with a time resolution of 100 Hz for turbulence analysis, as described by *Bögel and Baumann* [1991] and *Hauf* [1993]. We do not use airborne humidity measurements (Vaisala Humicap) because of their limited accuracy and the strong natural variability of ambient humidity. The role of ambient humidity for secondary-wake formation will thus be investigated in our subsequent work by treating ambient humidity as a free parameter.

3. Measurement Results

The measurements analyzed in this work were performed during the campaign CONTRAIL on April 22, 1996, near Augsburg, Germany. A B-747 aircraft flew at 1237 UTC over the measurement site of the ground-based lidar located at 48.3°N, 10.7°E, 500 m above sea level (asl). A cross-section measurement of the contrail was performed within the vortex phase by ground-based scanning lidar. The research aircraft FALCON performed in situ measurements of temperature, wind speed, and turbulence during an ascent across the flight level of the B-747, close to the lidar measurement in time (Δt ≈ min) and horizontal geographical location (Δx, Δy ≈ 10 km).

3.1. Aircraft Parameters

The lidar measurements presented below were performed on the contrail of a B-747-400 aircraft owned by Singapore airlines which was on its way from London to Singapore. For an overview of the aircraft data, see Table 1. We estimate the takeoff weight from the sum of the dry operating weight, the actual cargo/mail load, the actual passenger load, the actual baggage load, and the estimated takeoff fuel load. Since no direct information on the actual takeoff fuel load was available, we performed an interpolation using data from further available flights of this aircraft on the same flight route. To estimate the actual weight above our observation site near Augsburg, Germany, we assume a flight duration of 1 hour after takeoff in London. With an average fuel consumption of 13000 L/h and the specific weight of kerosene (800 kg/m^3 at 15°C) we obtain a fuel-weight reduction over Augsburg by 10,400 kg. Because of the increased fuel consumption during the initial ascent we use a fuel-weight reduction of 15,000 kg and thus obtain an estimated total weight above our observation site of 344,869 kg. The flight altitude is determined by the ground-based lidar. The true airspeed v_t is determined by subsequent CCD imaging and graphical analysis of both the wind-drift velocity vector v_w at the contrail altitude and the apparent velocity vector of the aircraft v_a (for technical details, see also section 2). We obtain v_a = (273.5 ± 2 m/s, 104.8°) and v_w = (26.5 ± 4 m/s, 95.8°), where north corresponds to 0°, and east corresponds to 90°. From this we finally derive the true airspeed v_t = (247.5 ± 5 m/s, 105.8°).

3.2. Ambient Atmosphere

The measured properties of the ambient atmosphere close to the visible contrail of the B-747-400 investigated in this work are listed in Table 2. The contrail was formed at an altitude of 10,171 in asl (lidar measurement) corresponding to a pressure of 263.7 hPa and a temperature of −52.3°C (FALCON data, see below). From this we calculate for the density of air ρ_{air} = 0.41 kg/m^3 at flight level. The tropopause had been at the 210 hPa level corresponding to an altitude of 11,570 m asl and a temperature of −65°C according to the 1200 UTC Munich radiosonde (≈50 km to the southeast of our measurement site).

3.2.1. Stratification.
We find from the airborne in situ temperature measurements of the FALCON that the contrail had been in a layer with a high variability of potential temperature with altitude (Figure 2). From a linear fit within the vertical domain of the observed contrail (section 3.3, Plate 1a) we find a slightly non-stably-stratified region (Figure 2). A vertical gradient of the potential temperature of $d\Theta/dz$ = −0.001 ± 0.0008 K/m is found, i.e., an imaginary Brunt-Väisälä frequency N with N^2 = (g/Θ_0) $d\Theta/dz$ = −3.0 × 10^{-5} ± 2.4 × 10^{-5} s^{-2}, where g = 9.81 m/s^2. The high standard deviation results from the high variability of Θ (see above).

Table 1. Data of Aircraft

Aircraft Type[a]	Boeing 747-400
Destination[a]	London-Singapore
Airline[a]	Singapore airlines
Aircraft registration[b]	9V-SPF
Engine type[b]	Pratt & Whitney PW4056
Average fuel consumption[c]	13000 L/h
Wing span[c]	64.44 m
Wing aspect ratio[c]	7.7
Maximum take-off weight[b]	394,625 kg
Maximum passenger capacity[b]	395
Dry operating weight[b]	183,641 kg
Actual cargo/mail load[b]	9623 kg
Actual passenger load (206 + 2 infants)[b,d]	15,525 kg
Actual baggage load[e]	8280 kg
Estimated actual takeoff fuel load[f]	142,800 kg
Estimated actual takeoff weight[f]	359,869 kg
Estimated weight above contrail measurement site[f]	344,869 kg
Flight level above measurement site[f,g]	10,171 m asl
Measured true airspeed above measurement site[f,g]	247.5 ± 5 m/s
Heading[h]	105.8°

[a]Munich Radar, personal communication.
[b]Singapore Airlines, London, personal communication.
[c]Taken from *Jackson et al.* [1997].
[d]Using 75 kg per person.
[e]Assuming 40 kg per person.
[f]For details, see text.
[g]Derived from ground-based lidar/CCD imaging.
[h]North corresponds to 0°, east corresponds to 90°.

3.2.2. Vertical shear of horizontal wind speed. In Figure 3 the horizontal wind speed S is plotted versus altitude as measured in situ by the FALCON. From a linear fit within the vertical range of the observed contrail (section 3.3, Plate 1a) a vertical shear of total horizontal wind speed of $dS/dz = -0.01 \pm 0.004$ s^{-1} is found. Effective shear, i.e., shear in right angle to the contrail, is smaller by a factor of 6 (heading of aircraft 105.8°, vector of horizontal wind at flight level 95.8°; see section 3.1). Together with the stratification result from Figure 2 a bulk Richardson number $Ri = N^2/(dS/dz)^2 = -0.3 \pm 0.3$ is obtained.

3.2.3. Ambient turbulence. We characterize the turbulent state of the atmosphere by in situ turbulence measurements onboard the research aircraft FALCON. The wind velocity components for the east-west (u), north-south (v), and vertical (w) directions are recorded at 100 Hz [*Bögel and Baumann*, 1991; *Hauf*, 1993]. For analysis we extracted the 1 min time interval during which the FALCON had been at the altitude of the contrail investigated by lidar (10,050–10,200 m, section 3.3, Plate 1a). From this time series the mean variances of the velocity fluctuations of the three wind components are calculated, $\langle u'^2 \rangle = 0.865$ m^{2}s^{-2}, $\langle v'^2 \rangle = 0.827$ m^2 s^{-2},

$\langle w'^2 \rangle = 0.250$ m^2 s^{-2}, where u', v', w' are the deviations from the 1 min mean values. This shows in our case study a slight anisotropy of air motions with the horizontal variances being approximately a factor of 3.5 larger than the vertical variance. Much stronger anisotropies (factor of 10 between horizontal and vertical variances) have been classified as being typical for the cruise altitude from a measurement campaign in the North Atlantic flight corridor [*Schumann et al.*, 1995]. According to *Pasquill and Smith* [1983] the observation of relatively larger vertical velocity variances in our case is in agreement with the moderately unstable atmosphere ($Ri = -0.3 \pm 0.3$; see above) compared to the typical, i.e., stably stratified atmosphere ($Ri > 10$) analyzed by *Schumann et al.* [1995].

To investigate the scale dependency of the anisotropy, we calculate the spectral density functions S_u and S_w, respectively (in m^3 radian^{-1} s^{-2}), as a function of wavenumber k (in radian/m). (The wavenumber scale was calculated from the measured frequency scale f using $k = 2\pi f/V_F$, where V_F is the speed of the FALCON). The spectra are calculated for the 1 min time interval (see above) by fast Fourier transformation. In Figure 4 the ratio of S_u to S_w is plotted versus wavenumber.

Table 2. Parameters of the Ambient Atmosphere of the Contrail

Tropopause[a]	11,570 m asl, $p = 210$ hPa, $T = -65°C$
Flight level	10,171 m asl, $p = 263.7$ hPa, $T = -52.3°C$, $\rho_{air} = 0.41$ kg/m^3
stratification	$d\Theta/dz = -0.001 \pm 0.0008$ K/m, $N^2 = -3.0 \times 10^{-5} \pm 2.4 \times 10^{-5}$ s^{-2}
vertical shear[b]	$dS/dz = -0.01 \pm 0.004$ s^{-1}
Richardson number	$Ri = -0.3 \pm 0.3$
ambient turbulence	inertial range $k = 0.004 - 0.1$ radian/m, $\varepsilon_{vert} = 7.4 \times 10^{-5} \pm 0.5 \times 10^{-5}$ m^2 s^{-3}

From ALCON in situ measurements close to the lidar contrail measurement ($\Delta t \approx$ min, Δx, $\Delta y \approx 10$ km).
[a]According to the Munich radiosonde ≈ 50 km to the east.
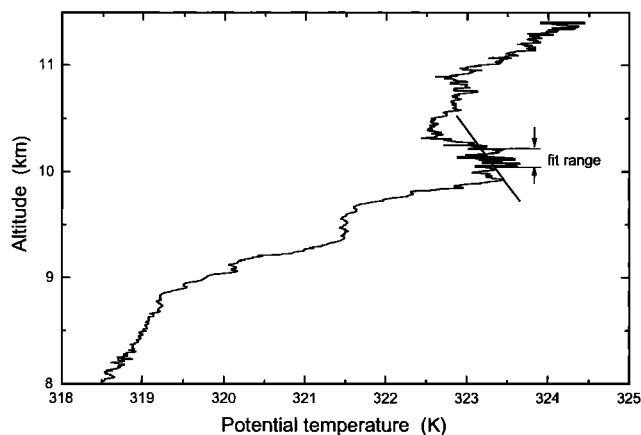[b]Shear of total horizontal wind speed; for effective shear, see text.

Figure 2. Vertical distribution of potential temperature measured during an ascent of the research aircraft FALCON nearly coincident in time and geographical location to the lidar measurement of Plate 1. The vertical fit range indicated corresponds to the vertical extension of the vortex phase wakes (Plate 1a). A vertical gradient of potential temperature of $d\Theta/dz = -0.001 \pm 0.0008$ K/m is found.

The figure shows locally isotropic turbulence in the intermediate wavenumber range, as indicated by the fitted line. Only for $k < 0.004$ radian/m S_u decays significantly stronger than S_w with k and does not support an "inertial range" assumption.

Figure 5 shows the spectral density function $M(k) = k$ $S_w(k)$. The spectrum is following a $M \propto k^n$ power law with $n = -0.69 \cong -2/3$ in the wavenumber range $k = 0.004$–0.1 radian/m, as indicated by the fitted line. Again, as from the findings of Figure 4, this corroborates an inertial range assumption with an active flow of turbulent energy from low to high wavenumbers. For the inertial subrange indicated in Figure 5 we compute for our case study the vertical eddy dissipation rate $\varepsilon_{vert} = 2\pi f V_F^{-1}[M(f)/c_k]^{3/2} = 7.4 \pm 0.5 \times 10^{-5}$ m^2 s^{-3}, using the Kolmogorov constant $c_k = 0.66$ [*Saddoughi and Veeravalli*, 1994]. This result during our case study above southern Germany is within the order of magnitude expected climatologically [*Tank*, 1994], but is approximately a factor of 1000 higher than typical values above oceans reported by *Schumann et al.* [1995].

3.3. Lidar Analysis of the Contrail

All contrail parameters derived in the following sections are summarized in Table 3. The information presented below is derived from 30 lidar profiles (10 laser pulses each) measured for 30 subsequent lidar zenith angles ranging from 54.4° to 57.3° during a time span of 5.7–77.4 s behind the wing of the aircraft. For a typical extinction profile that results from the ice particle distribution across the center of one wingtip vortex, see Figure 6. The extinction profiles are calculated from the lidar backscatter signal using calibration to a Rayleigh backscatter profile that is calculated on the basis of radiosonde pressure-temperature data. For the inversion of the measured attenuated backscatter signal a lidar ratio (extinction-to-backscatter ratio) of $LR = 65$ is used. It is derived independently from the lidar measurements using complementary data from shadow calibration, as explained in section 3.3.3.

3.3.1. Vortex descent. The pair of trailing vortices behind an aircraft has a downward impulse that balances the weight of the aircraft. This vertical motion is assumed to be influenced by

aircraft parameters as well as by atmospheric stratification. We derive the vortex descent rate from 16 of our 30 lidar profiles that show a backscatter signal from the ice within the down-traveling vortex pair (10.8–47.8 s behind aircraft; see, for example, Figure 6). Correcting for horizontal wind drift and changing lidar zenith angles we obtain the altitudes of the 16 backscatter maxima due to the ice within the vortex pair as displayed in Figure 7. The two down-traveling wingtip vortices are penetrated by the lidar one after the other (lidar zenith angles near 57°). Thus we obtain altitude information first for one of the descending vortices and then for the other. Only part of the lidar profiles penetrated both vortices (Figure 6). For clarity, in Figure 7 the left and right vortex data are offset in altitude. In the top part of Figure 7 we combined right and left vortex altitude data (no offset). The arithmetic mean is used where coincident data exist for both vortices. To derive these absolute altitudes, we assumed that the vortex pair had not been tilted, although a roll of a vortex pair has been reported to be possible in principle both in sheared and non-sheared media [*Sarpkaya and Daly*, 1987]. Under the assumption that there was no tilt a slight increase of the descent rate is recognized (Figure 7), i.e., a value of -2.5 ± 0.1 m/s in the early part of the measurement (linear regression to the first 5 data points, i.e., 10.8–20.6 s behind the aircraft), and an increased value of -3.1 ± 0.1 m/s later on (linear regression to data points 6–16, i.e., 23.1–47.8 s behind aircraft).

These lidar-derived descent-rate values are on the higher end of the mean vortex descent rates reported previously for B-747 aircraft [*Schumann*, 1994; *Schumann et al.*, 1995]. We calculate the theoretical estimate for the initial downward velocity based on the Kutta-Joukowski law (see, for example, *Schumann et al.* [1995] for details) using $w_{ini} = -8W\pi^{-3} \rho_{air}^{-1}B^{-2}V^{-1}$, where W is the weight of aircraft, ρ_{air} is the density at flight level, B is the wing span, and V is the true airspeed of the aircraft. Using our actual data of Table 1 and ρ_{air} at the flight level from section 3.2 (Table 2), we obtain the theoretical estimate $w_{ini} = -2.05$ m/s for the initial downward velocity. This could be compared with our lidar-derived value of -2.5 m/s for the interval 10.8–20.6 s behind the aircraft. We discuss two possible reasons for this 22% discrepancy between measured and calculated downward velocities. (1) There could be already an increase of the initial downward velocity within the first 10.8 s (in addition to the measured increase later on, see above). This could be caused by the fact that the vertical domain of our contrail had been within a layer of slightly unstably stratified atmosphere (section 3.2). Unstable stratification has been found to be a possible reason for an increasing descent speed from theoretical studies [e.g., *Greene*, 1986; *Schilling et al.*, 1996]. (2) Another contribution to the underestimation of the measured downward velocity by the theoretical equation for w_{ini} can be as follows: Neglecting detrainment of fluid from the wingtip vortices (see section 4) means neglecting that the vortices have to approach each other due to reduced pressure at the center of the vortex system. Vortex approach can contribute to an increased downward velocity, as pointed out by *Scorer and Davenport* [1970] (separation enters into the descent velocity squared). In our case we measured a vortex separation of 47 ± 5 m (see next paragraph) which is 8% smaller than the result from a simple theoretical estimate neglecting detrainment and vortex approach (i.e., 50.6 m; see next paragraph). This 8% discrepancy in vortex separations contributes 16% to the velocity discrepancy. Thus using the measured (reduced) vortex separation, the 22% velocity dis-
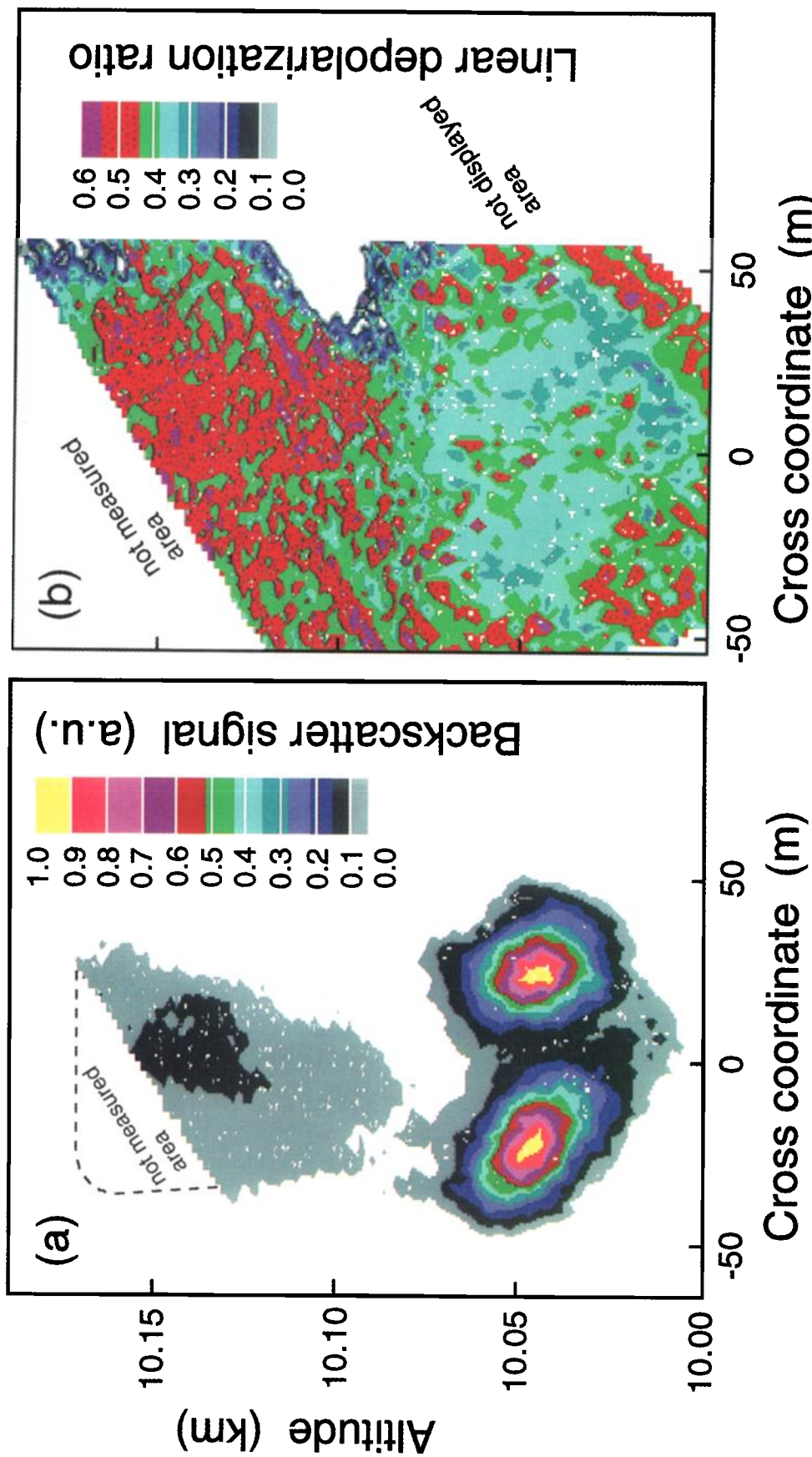
Plate 1. (a) Scanning lidar cross section of the backscatter signal of the contrail of a B-747-400 in the vortex regime showing the secondary-wake phenomenon (same contrail as in Figure 1). The image represents the vertical contrail evolution ≈50 s behind aircraft. For details, see text. (b) Same cross-sectional domain showing the distribution of linear depolarization ratio.
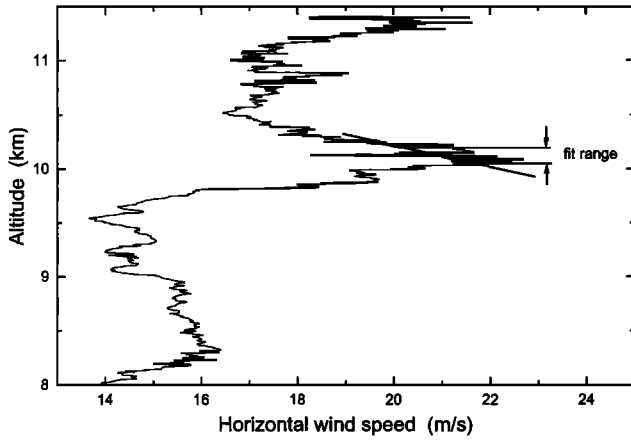
Figure 3. Vertical distribution of total wind speed measured during an ascent of the research aircraft FALCON nearly coincident in time and geographical location to the lidar measurement of Plate 1. The vertical fit range corresponds to the extension of the vortex phase wakes (Plate 1a). A vertical shear of total wind speed of $dS/dz = -0.01 \pm 0.004$ s^{-1} is found.

Figure 5. Spectral density function $M(k) = kS_w(k)$ of vertical velocity fluctuations over wavenumber k measured during a 1 min flight segment of the research aircraft FALCON at the altitude of the lidar-measured contrail (Plate 1a) and nearly coincident in time and geographical location to the lidar measurement (same flight segment as in Figure 4).

crepancy between the Kutta-Joukowski result and the measurement (see above) reduces (by 16%) to 6%, which is not too far from the 4% measurement error for the descent velocity (Table 3).

3.3.2. Cross-sectional backscatter image. A cross-sectional image of the contrail within the vortex phase is obtained from the lidar backscatter signal (Plate 1a). This image is constructed from our 30 side-by-side lidar profiles (see, for example, Figure 6) using graphical interpolation. For this the descent migration of the vortices has to be taken into account as well as the horizontal wind drift and the different angles of the lidar-pointing directions. The contrail was penetrated by the lidar starting from the lower edge (first lidar profile, 5.7 s behind aircraft) scanning toward the upper edge (30th lidar profile, 77.4 s behind aircraft). To obtain a symmetrical image of the two descending vortices, we corrected for the vortex
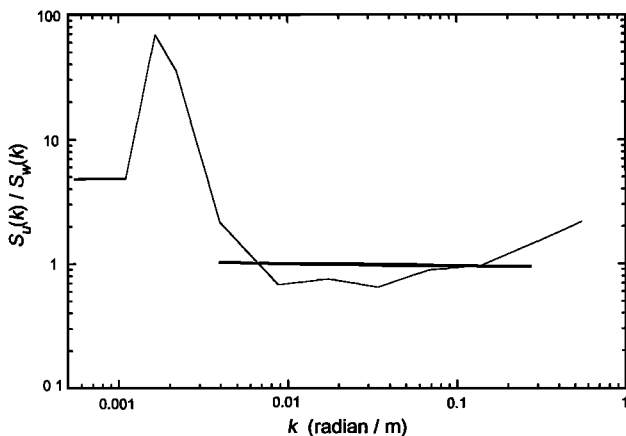
descent by vertical shifting of the first 19 lidar profiles (5.7–50.3 s behind aircraft) according to their actual descent (as has been given in Figure 7). This correction was not applied for the area above the vortices (20th–30th lidar profile, 50.3–77.4 s behind aircraft) which shows a characteristic feature, i.e., the secondary wake. The shifting correction is not necessary there because the secondary wake is left behind the descending vortices; that is, it does not perform a descending motion and stays on a constant vertical level to a good approximation (neglecting distortions by the wind field during the 50.3–77.4 s time period). We point out that because of this method of constructing the cross-sectional image, Plate 1a shows a good approximation of the vertical evolution of the contrail at ≈50 s behind the aircraft.

Plate 1a (≈50 s behind aircraft; see above) displays a pair of wingtip vortices marked by ice (primary wake) and, additionally, a diffuse secondary wake above. The strongest backscatter signal in Plate 1a is clearly seen at the centers of the vortex cores. We point to a smooth distribution of the backscatter signal across the center of the vortices. Even as early as 23.1 s

Table 3. Experimental Contrail Properties

	Primary Wake	Secondary Wake
Descent rate, initially[a]	-2.5 ± 0.1 m/s	•••
Descent rate, finally[b]	-3.1 ± 0.1 m/s	•••
Vortex separation[c]	47 ± 5 m	•••
Vertical extension[c]	160 m	160 m
Vertical wake-gap[d]	onset after ≈50 s	onset after ≈50 s
Cross-sectional area[c,d]	4620 m^2	4410 m^2
Depolarization ratio[e]	0.35	0.5[d]
Lidar ratio[f]	65	65
Maximum OT[g]	1.18	0.24
$\int$OT(r) dr^d	52 m	10 m

[a] Average for 10.8–20.6 s behind aircraft.
[b] Average for 23.1–47.8 s behind aircraft.
[c] Approximately 50 s behind aircraft.
[d] For details, see text.
[e] Linear depolarization ratio; for definition, see text.
[f] Extinction-to-backscatter ratio at 532 nm.
[g] OT, optical thickness; r is perpendicular to the contrail and lidar axes.

Figure 4. Ratio of the spectral density functions of horizontal (S_u) and vertical velocity fluctuations (S_w) over wavenumber k measured during a 1 min flight segment of the research aircraft FALCON at the altitude of the lidar-measured contrail (Plate 1a) and nearly coincident in time and geographical location to the lidar measurement. A wavenumber range with locally isotropic turbulence is found, as indicated by the fitted line.
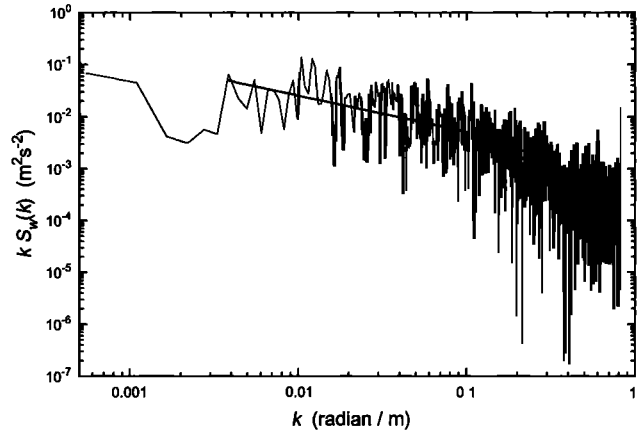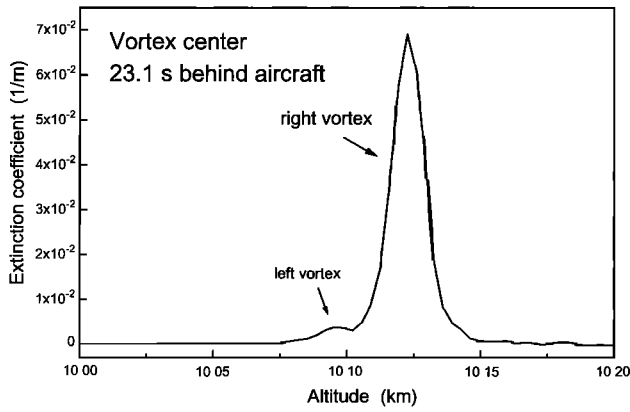
Figure 6. Extinction profile derived from a lidar backscatter profile (average of 10 laser pulses) penetrating one vortex wake of a B-747-400 through its center 23.1 s behind aircraft (same contrail as in Figure 1).

Figure 8. Optical thickness of the contrail of a B-747-400 along 30 subsequent lidar profiles recorded in the time period of 5.7–77.4 s behind aircraft with lidar zenith angles ranging between 54.4° and 57.3° (same contrail as in Figure 1).

behind aircraft there is a smooth Gaussian-like distribution of the extinction coefficient across each vortex (Figure 6). The jets have completely lost their individuality and are mixed completely within the vortices at this stage. The highest altitude backscatter feature which is enhanced compared to the background level is found at 10,171 m asl. We take this as the flight level (Table 1). We find a vertical extension of $\sigma_z = 160$ m (after $\approx$50 s; see above) and a spacing of the vortex cores of $D = 47 \pm 5$ m. This is in good agreement with the theoretical vortex separation of $D = 50.6$ m we calculate from the span width $B = 64.44$ m of a B-747-400 using $D = \pi B/4$, in particular when considering the mutual approach of the two vortices due to detrainment, as outlined above [*Scorer and Davenport*, 1970].

We derive from Plate 1a the cross-sectional areas of the secondary wake and the primary wake $\approx$50 s behind the aircraft (see above). At this time the areas enclosed by the contour of a backscatter signal of 0.1 (grey-colored level in Plate 1a) are 4410 m² for the secondary wake and 4620 m² for the primary wake. *Schumann* [1994] estimated an effective cross
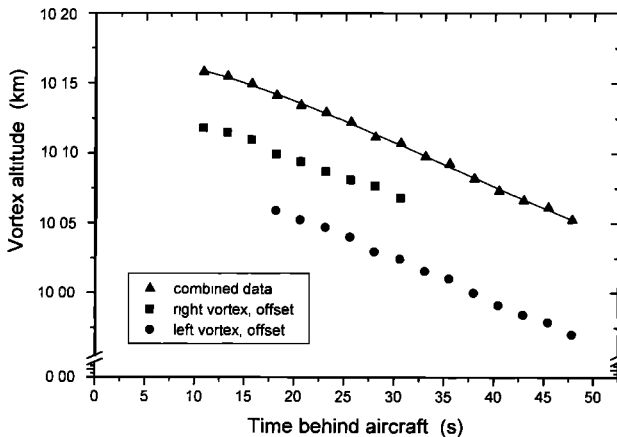

Figure 7. Ground-based lidar measurement of the descent of the pair of trailing vortices behind a B-747-400 aircraft, by 16 subsequent lidar profiles (same contrail as in Figure 1). Altitudes of the fight and left wingtip vortex, respectively, were obtained subsequently with some overlap. The combined data points are connected by a third-order polynomial fit.
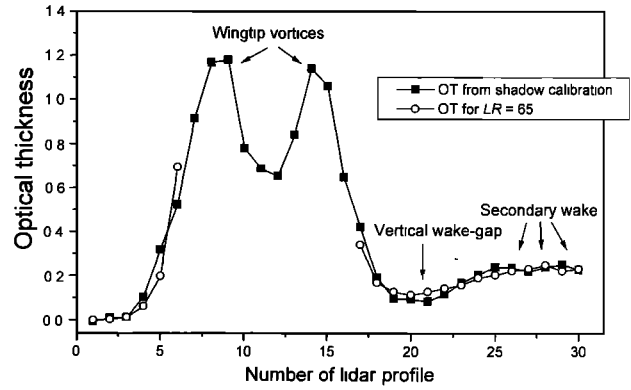
section of 3600–5400 m² due to the jets at the beginning of the vortex regime (after 10 s) and a growth of the trailing vortex pair to 21000–52000 m² at the end of the vortex regime (after 2–3 min) behind a B-747 based on simple analytical models. Interpolating these data results in a cross-sectional area of the vortex pair of 7700–16500 m² at $\approx$50 s behind a B-747. Compared to our measurement result of 4620 m², there seems to be an overestimation of cross-sectional growth by this simple model. We do not perform at this place a comparison to one of the more detailed models [*Quackenbush*, 1996; *Lewellen and Lewellen*, 1996; *Gerz and Ehret*, 1996, 1997; *Schilling et al.*, 1996] which address both the confinement process in the primary wake due to the vortex system and the detrainment. Instead, we suggest these models be run with the detailed input data given here for such a comparison.

3.3.3. Optical thickness. The relative magnitude of our measured cross-sectional areas of the secondary wake and the primary wake are $\sim$1:1 at $\approx$50 s behind aircraft (see above). However, the maximum backscatter signal from the secondary wake is a factor of 10 weaker than that of the primary wake. For a further characterization of both domains we derived the optical thickness (OT) along the 30 different lidar directions, as displayed in Figure 8. The OTs are derived using the shadow calibration technique [*Ruppersberg and Renger*, 1991], see squares in Figure 8. To determine the lidar ratios (extinction-to-backscatter ratios), the OTs are additionally calculated independently from the integral over the extinction profiles assuming an a priori lidar ratio. The resulting OTs (circles in Figure 8) are compared to the OTs derived from shadow calibration. This procedure is iterated for varied lidar ratios till a best fit in OTs is obtained, and here a lidar ratio of $LR = 65$ was found (Figure 8). It can be seen that the maximum OT at the vortex cores (OT $\approx$ 1.18) is high compared to the OT across the secondary wake (OT $\approx$ 0.25).

For a measure of the relative magnitude of the ice surface areas within the secondary wake and the primary wake, respectively, we use the quantity $I = \int OT(r) \, dr$ (in meters) for each regime. Here r is a coordinate (in meters) within the cross-sectional plane of the contrail and perpendicular to the lidar direction. This integral is identical to $I = \int \sigma_{ext}(x, z) \, dx \, dz$, i.e., to the cross-sectional integral of the extinction coefficient σ_{ext} (in m⁻¹) of the contrail, where x (in meters) is a horizontal coordinate perpendicular to the flight direction, and z (in

meters) is a vertical coordinate. For the typical ice particles of contrails it holds the following: $\sigma_{ext} \propto IWC/r_{eff}$, where IWC is the ice water content (in g/m^3) and r_{eff} (in meters) is the effective radius of the ice particle size distribution [*Ebert and Curry*, 1992]. The ice mass is to a good approximation linearly related to r_{eff}^3 and the ice surface area to r_{eff}^2. Hence calculating I_v for the primary wake and I_s for the secondary wake, we obtain a ratio I_v/I_s for the ice surface areas of these two different domains. Using Plate 1a and Figure 8, we calculate $I_v = 52$ m and $I_s = 10$ m; that is, we derive a ratio of ice surface areas of 5:1 for the primary wake and the secondary wake, respectively, at ≈ 50 s behind aircraft. This ratio strongly depends on the distance behind aircraft as well as on ambient humidity, as will be shown in our subsequent work [*Sussmann and Gierens*, this issue].

Our measurement results can be compared to recent numerical simulations where a time series of the exhaust mass in the secondary wake has been related to the total exhaust mass [*Gerz and Kärcher*, 1996]. From this the respective entrainment rates, as they are used in chemical box models, were calculated. A significant drop of the entrainment rate of the primary wake has been found during the vortex phase with an increase when the vortices collapse [*Gerz and Kärcher*, 1996]. Generally, the simulations showed about 70% of the total exhaust mass to be stored in the primary wake, which might be related to our 5:1 ratio of IWC/r_{eff} after ≈ 50 s (see above). However, we note that for these calculations, passive tracers were used. The results can therefore, in a strict sense, not be transferred to the ice masses, which are influenced by dynamic phenomena favoring ice growth or evaporation locally within the contrail. In particular, we note that in contrast to the simulations, we do not find an increase of the ice mass of the primary wake at the end of the vortex phase. Rather, we find in most cases a disappearance of the visible wingtip vortices and a further persistence of only the secondary wake. This will be detailed in our subsequent paper [*Sussmann and Gierens*, this issue].

3.3.4. Vertical wake-gap. Here we want to mention a phenomenon we call the "vertical wake-gap." The phenomenon has not hitherto been described in the literature and not been found from modeling studies. In Plate 1a a vertical wake-gap between the secondary wake and the wingtip vortices is apparent. We found the vertical wake-gap in the exhaust distribution to have a distinct onset within the vortex phase typically at $\approx 40-50$ s behind aircraft (this will be detailed in our subsequent work [*Sussmann and Gierens*, this issue]), while there is a continuous curtain of exhaust down to the wingtip vortices before. The vertical wake-gap can also be nicely seen from the vertical distribution of the optical thickness plotted in Figure 8. We found this vertical wake-gap to occur regularly from observation of hundreds of contrails via eye.

A vertical wake-gap did not result from numerical simulations of detrainment, showing a continuous curtain of fluid down to the vortex pair up to the end of the vortex regime [*Gerz and Ehret*, 1996; *Schilling et al.*, 1996]. This is probably due to the fact that passive tracers were investigated in these simulations. We found the origin of the vertical wake-gap to be due to the dynamics affecting the evolution of the ice particles locally. In this context we note that in the contrail investigated here, only the secondary wake became persistent. The wingtip vortices disappeared at the end of the vortex phase, as already pointed out in section 3.3.3. This phenomenon is typical for four-engined aircraft and will be investigated together with the

mechanism of the vertical wake-gap in our subsequent work [*Sussmann and Gierens*, this issue].

3.3.5. Linear depolarization ratio. The linear depolarization ratio is defined as $\delta = I_\parallel/I_\perp$, where the backscattered intensities parallel polarized ($I_\parallel$) and cross-polarized ($I_\perp$) with respect to the laser field are measured by two photomultipliers with perpendicular polarization orientations. Plate 1b displays the lidar-derived linear depolarization ratio in the same cross-sectional measurement domain as shown before (approximately 50 s behind aircraft; for details, see discussion of Plate 1a). The depolarization ratio within the primary wake is significantly below the value of 0.5 found for natural cirrus [*Sassen*, 1991] and aged persistent contrails. This can be explained in terms of the particles within the vortices being much smaller than the lidar wavelength (532 nm) or close to spherical [*Mishchenko and Travis*, 1994]. Obviously, the particles within the wingtip vortices are well isolated from the ambient atmosphere, and thus (nonspherical) crystal growth is prevented.

The depolarization ratio in the areas around the vortex pair and in the secondary-wake domain above is close to 0.5 typical for (aged) hexagonal crystals (Plate 1b). This result cannot be due to a possible subvisible background cirrus. We find from the individual lidar backscatter profiles (see also Plate 1a) that the backscatter signal of the secondary wake exceeds any possible background signal by orders of magnitude. Hence the 0.5 depolarization ratio is due to material detrained from the primary wake. This provides evidence that at the moment of the measurement the particles in the secondary wake had already run through a phase of nonspherical growth. This is due to mixing with ambient air that is supersaturated with respect to ice.

4. Mechanisms of Secondary Wake Formation

Figure 1 and Plate 1a display, above the vortex pair, the so-called secondary wake. We discuss five different mechanisms given in the literature which possibly can contribute to secondary-wake formation, i.e., (1) "aircraft-wake-induced ice cloud formation," "detrainment," which we classify as being due to (2) "baroclinic detrainment," (3) "shear detrainment" and (4) "turbulent detrainment," and (5) "nonentrainment." In sections 4.1–4.5 we investigate the relative importance of these mechanisms for the formation of the secondary wake of the case study discussed above.

4.1. Aircraft-Wake-Induced Ice Cloud Formation

In a recent numerical study of aircraft-wake-induced ice cloud formation the engine exhaust has been excluded from the simulations in order to study cloud formation due to aerodynamic effects [*Gierens and Ström*, 1998]. The authors found the possibility of ice formation via homogeneous freezing nucleation of ambient haze droplets in the upwelling limbs of the vortex pair for an ambient humidity strongly supersaturated with respect to ice.

We exclude this possible mechanism being responsible for the early onset of the secondary wake in our case study after ≈ 4 s, since *Gierens and Ström* [1998] found that the nonexhaust ice cloud does not form earlier than about 60–100 s behind aircraft. This is more than an order of magnitude later than the onset of the secondary wake that we found in this work as early as 1040 m (4.2 s) behind aircraft (see section 4.5). However, the mechanism can, in principle, have contributed to secondary-wake growth at later stages in the contrail evolution.

4.2. Baroclinic Detrainment

In several theoretical (few experimental) investigations it has been found that the vortex evolution strongly depends on stratification [*Scorer and Davenport*, 1970; *Greene*, 1986; *Quackenbush et al.*, 1996; *Schilling et al.*, 1996]. Baroclinic detrainment [*Scorer and Davenport*, 1970], i.e., detrainment due to the baroclinic torque which results from the vortex descent in a stratified atmosphere, has up to now generally been considered as the main reason for detrainment.

We first evaluate the baroclinic detrainment mechanism with respect to the observed early onset of the secondary wake. The baroclinic torque originates as early as the vortices start their descending motion leading to detrainment. However, according to numerical simulations, assuming a weakly stratified atmosphere, a secondary wake is expected to become visible by this mechanism later than typically 50 s behind a B-747; see Figure 8 in the work of *Gerz and Kärcher* [1996]. Therefore we conjecture that it is not baroclinic detrainment that initially caused the observed early onset of the secondary wake after ≈ 4 s in our case study, keeping in mind that stratification had not extraordinarily been strong.

Evaluating the possible role of baroclinic detrainment at later stages during the secondary wake growth, we found from the airborne in situ temperature measurements that the contrail had been in a layer of a weakly (nonstably) stratified atmosphere (Figure 2). A vertical gradient of the potential temperature of $d\Theta/dz = -0.001 \pm 0.0008$ K/m was found or $N^2 = (g/\Theta_0)\, d\Theta/dz = -3.0 \times 10^{-5} \pm 2.4 \times 10^{-5}\,\text{s}^{-2}$. We compare this to typical values. From a statistical analysis of ECMWF (European Center for Medium-Range Weather Forecasts) data the typical atmosphere was found to be stably stratified with N^2 peaking around $N^2 = 1.0 \times 10^4\,\text{s}^{-2}$ and $N^2 = 4.0 \times 10^{-4}\,\text{s}^{-2}$ for tropospheric and stratospheric cruising altitudes, respectively [*Dürbeck and Gerz*, 1996]. These values are about an order of magnitude larger than the (signless) value of $|N^2| = 3.0 \times 10^{-5}\,\text{s}^{-2}$ in our case study (see above). From this we conclude that there was only a minor contribution of baroclinic detrainment to secondary-wake growth in our observation as compared to typical cases.

4.3. Shear Detrainment

Robins and Delisi [1989] described in a numerical study the influence of coexisting stratification and vertical shear on the evolution of a vortex pair in water without taking turbulence effects into account. The results showed that the bulk Richardson number *Ri* (the ratio of stratification forces to shear forces) is an important parameter in the evolution. When *Ri* is large, the vortex pair evolves more or less symmetrically, and baroclinic detrainment (see above) dominates the evolution. When *Ri* is small, the vortices evolve asymmetrically, and the vortex with rotational sense opposite to that of the mean shear decays, while the other vortex survives. The result is a tilting of the vortex pair and a detrainment of upward moving fluid from one of the two vortices with the rotational sense opposite to the circulation that can be attributed to vertical shear [*Robins and Delisi*, 1989].

The question is whether shear did contribute quantitatively to the secondary-wake formation observed in our case study. We found within the vertical range of the observed vortex system a vertical shear of total wind speed of $dS/dz = -0.01 \pm 0.004\,\text{s}^{-1}$ (Figure 3). Together with the stratification result from Figure 2 a bulk Richardson number of $Ri = -0.3 \pm 0.3$ is obtained.

We estimate the quantitative contribution of the measured shear $dS/dz = -0.01 \pm 0.004\,\text{s}^{-1}$ to the evolution in our observed vortex system (Plate 1a). First, we state that effective shear, i.e., vertical shear in right angles to the contrail, is significantly smaller than this value (heading of aircraft 105.8°, direction of total wind speed 95.8°; $\tan(105.8°-95.8°) = 0.18$). The resulting velocity differences of horizontal wind at the upper and lower edges of the vortices are of the order of 0.1 m/s. This is significantly below the swirling velocities of the vortices (≈ 10 m/s). We conclude that vertical shear in our case study did not significantly contribute to secondary wake formation.

4.4. Turbulent Detrainment

The effects of turbulence upon vortex dynamics have been neglected in many theoretical studies, since investigations were based upon two-dimensional (2-D) numerical simulations. However, turbulence can influence vortex migration [*Greene*, 1986; *Sarpkaya and Daly*, 1987] and vortex decay (Crow instability and vortex bursting [*Crow and Bate*, 1976; *Spalart and Wray*, 1996]). Recently, the effect of both ambient turbulence and aircraft boundary layer turbulence on the detrainment mechanism have been investigated theoretically [*Gerz and Ehret*, 1996; *Gerz and Kärcher*, 1996].

We found in section 3.2 that ambient turbulence, measured close to the contrail of our case study, had been fully developed with locally isotropic turbulence and an inertial range in the 0.004–0.1 radian/m wavenumber domain; the vertical eddy dissipation rate $\varepsilon_{\text{vert}}$ exceeded typical values above oceans at cruising altitude by a factor of 1000 (Table 2).

The impact of such a relatively high $\varepsilon_{\text{vert}}$ is reflected, e.g., by the findings of *Sarpkaya and Daly* [1987], showing that both the descent and the demise of the vortices are controlled strongly by the dissipation rate of the background turbulence. Furthermore, it was shown recently by numerical simulations that ambient turbulence can significantly enhance the effect of baroclinic detrainment, leading to a much more diffuse and broader secondary wake [*Gerz and Ehret*, 1996] and an earlier onset of the secondary wake [*Gerz and Kärcher*, 1996]. These authors assumed typical ambient turbulence that was simulated by a three-dimensional field of weak, anisotropic, and decaying turbulence in a stably stratified atmosphere. This turbulence was found to trigger axial perturbations of the jet flow and thus lead to an enhanced detrainment. Aircraft boundary layer turbulence, although being 1 order of magnitude stronger than ambient turbulence, was found to play a minor role in general [*Gerz and Ehret*, 1996]. Comparing our turbulence parameters (Table 2) to the assumptions on typical turbulence conditions in these simulations, we find a stronger and fully developed turbulence in our experimental case study. The length scales of the energy containing atmospheric eddies within the inertial range of our turbulence spectrum (Figure 5) are of the order of ≈ 100 m. This is in the order of the wing span; that is, it is exceeding the vortex core diameter. This results in a strong capability to erode the organized vortex structure [*Gerz and Ehret*, 1996].

4.5. Nonentrainment Versus Early Detrainment

In recent work, the secondary wake in a photograph quite similar to the CCD image of Figure 1 was tentatively attributed to the postulated mechanism of nonentrainment of exhaust from the jet exhaust streams of the inner engines into the vortices [*Gerz and Ehret*, 1997, Figure 3]. This mechanism had
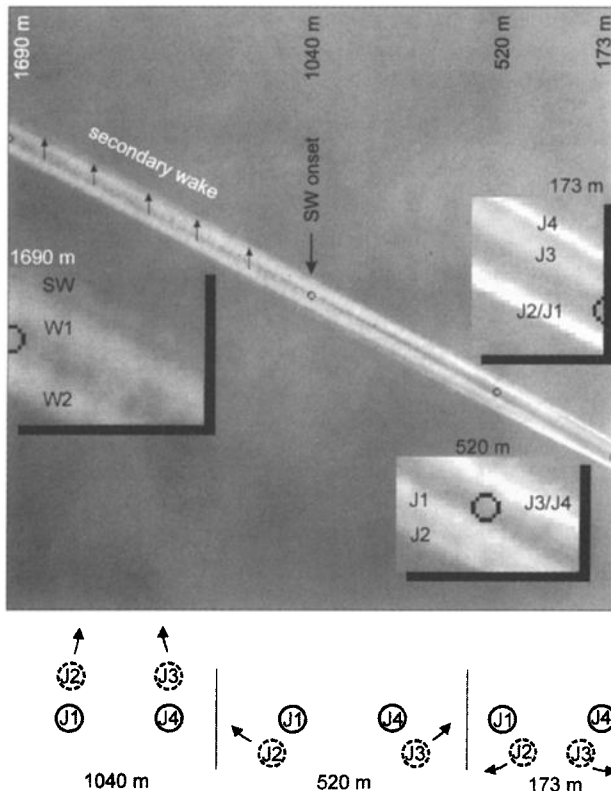
Figure 9. CCD image of the contrail of a B-747-400 in the transition between the jet and the vortex regimes (same contrail as in Figure 1). The four jets (labeled J1–J4 from left to right) are still separated but already wrapped by a one-eighth period around the vortices on the very right-hand side of the image (173 m behind aircraft; the jets J2/J1 seem to merge at this stage due to the 0.86 rad zenith angle of the observational direction; see schematics in the bottom part). A wrapping of a three-eighth period is clearly to be seen at 520 m behind aircraft. After a three-fourth wrapping period (1040 m, 4.2 s) the onset of the secondary wake (SW) becomes visible. (Because of the viewing angle geometry the indicated visible SW onset may be several hundred meters upstream). On the left-hand side of the image (1690 m) the two wingtip vortices (W1, W2) and the secondary wake are clearly discernable.

been postulated due to observations of an early onset of a secondary wake "immediately behind aircraft" by eye that was in disagreement with simulations of detrainment, where a secondary wake was found to become visible at significant later times (T. Gerz, personal communication, 1996). However, an open question remained, since a simulation of the postulated nonentrainment phenomenon could not be achieved in the theoretical studies by the authors, either for buoyant or non-buoyant exhaust [Gerz and Ehret, 1996, 1997]. (We point out that there exist three photographs of an instant onset of a "third wake" directly behind the body of two-engined aircraft probably caused by the Auxiliary Power Unit [Antesberger, 1996]; we do not consider this rather rare phenomenon here, this is not the typically occurring phenomenon that was tentatively explained by nonentrainment).

Instead of nonentrainment we found a different mechanism. From the CCD image in our Figure 9 the entrainment of the four jet trails into the vortices can be followed. At the very right-hand side of Figure 9 (173 m behind aircraft) it can be clearly seen that the inner jets (J2 and J3) have already

wrapped a one-eighth period around the outer jets (J1 and J4). (The viewpoint of the observer is important: the jets J2/J1 appear overlapping, see enlarged image parts and schematics in Figure 9). We clearly do not see the "nonentrainment phenomenon" at this stage, i.e., an escape of exhaust of the inner jets at the very beginning of the roll-up process of the wingtip vortices. Rather, the entrainment process continues, reaching a wrapping of the jet trails by a three-eighth period at 520 m behind the aircraft, as can be clearly seen in Figure 9, still without showing a secondary wake. (Because of the viewpoint of the observer, now the jets J3/J4 appear overlapping.) This observed wrapping of the jets into the vortices compares very well with the results from numerical modeling, as given by Gerz and Ehret [1997, Figure 5]. However, as early as 1040 m behind the aircraft in Figure 9 the onset of a secondary wake is seen starting to grow continuously above the primary wake. (Because of the viewing angle geometry the indicated visible secondary-wake onset may be several hundred meters upstream). This can be followed up to the left-hand side of the figure (1690 m behind aircraft). Starting from this stage, the continuously ongoing growth of the secondary wake can be followed by a video sequence not shown here (see our subsequent work [Sussmann and Gierens, this issue]). Extrapolating linearly the observed wrapping phases (one-eighth period at 173 m and a three-eighth period at 520 m; see above), we find that the observed secondary-wake onset at 1040 m (4.2 s) corresponds to a stage where the jets of the inner engines are wrapped a three-fourth period around the corresponding jets of the outer engines; that is, the jets of the inner engines are located exactly above the jets of the outer engines (see schematics in the bottom part of Figure 9). According to this observation the onset of the secondary wake is due to an early detrainment of fluid stemming essentially from the jets of the inner engines at the beginning. We assume an increasing contribution to the secondary wake from the outer-engine exhaust later on. This is because mixing within the vortices leads to a homogeneous Gaussian-like distribution of ice concentration across each vortex as early as ≈20 s behind aircraft (see extinction profile of Figure 6).

The important finding of this section is (1) that the observed visible secondary-wake onset after ≈4 s is not immediately behind aircraft ("nonentrainment") and (2) that the onset is much earlier than hitherto expected from the analysis of the baroclinic detrainment and turbulent detrainment mechanisms by numerical studies (onset not before typically 25 s behind aircraft [Gerz and Kärcher, 1996]; see sections 4.2, 4.4, and 4.5). This finding is not restricted to our present case study. Rather, we learned from visual observation of hundreds of contrails [Sussmann and Gierens, this issue] that an early secondary-wake onset after a few seconds behind aircraft is typical for B-747 aircraft in general.

We conjecture that the observed early onset of the secondary wake after ≈4 s is due to turbulent detrainment. This is based (1) on our above exclusion of all other possible and relevant formation mechanisms (sections 4.1–4.5) and (2) on the fact that it has been shown, in principle, that ambient turbulence can shift the secondary-wake onset toward earlier times compared to cases where only baroclinic detrainment is present [Gerz and Kärcher, 1996].

5. Conclusions and Outlook

This paper gave insight into the mechanisms of vertical contrail dispersion during the vortex phase. This vertical disper-

sion strongly determines the vertical extension of a contrail during its total life span, since for timescales larger than minutes, the plume spreads mainly horizontally by shear and turbulence in the ambient air.

The details of vortex phase dispersion are of relevance for chemical modeling in the exhaust plume as well. Chemical transformation of exhaust trace species, which has been modeled for single jets [Kärcher et al., 1996a], is influenced by the vortex system due to the strong coupling of mixing and chemistry [Gerz and Kärcher, 1996]. In chemical box models an accurate knowledge of the entrainment rates is essential [Kärcher et al., 1996b], especially in case of diffusion-limited reactions [Stockwell, 1995].

We presented for a vortex phase contrail of a B-747 a closed experimental data set. It included all relevant aircraft parameters together with data on the cross-sectional evolution and the optical properties of the contrail, and all atmospheric parameters relevant for the dynamic evolution. This data set provides a basis for testing and improving the modeling of vortex downward migration and vertical contrail dispersion, detrainment mechanisms, and entrainment rates. This case study was complemented by extensive observations via eye.

On the basis of the experimental data of our case study we performed an analysis of the different physical mechanisms reported in the literature so far which could possibly explain the formation of a diffuse secondary wake above the primary wake. The mechanism of "aircraft-wake-induced ice cloud formation" cannot be attributed to the observed early onset of the secondary wake after ≈ 4 s; however, it could, in principle, have contributed to secondary-wake growth later in the vortex regime. The mechanisms of "baroclinic detrainment" and "shear detrainment" were found to contribute relatively weakly to secondary-wake formation in the case studied, whereas ambient turbulence was found to have a strong potential to enhance secondary-wake formation via "turbulent detrainment." We could exclude the mechanism of "nonentrainment" of exhaust into the vortices as being responsible for the observed early onset of the secondary wake after ≈ 4 s in our case study. By exclusion of all other relevant formation mechanisms this early secondary-wake onset is conjectured to be due to turbulent detrainment.

We point to three observational phenomena typical for contrails of four-engined aircraft which have not been found from theoretical considerations and numerical modeling, i.e., (1) the early visible onset of the secondary wake (≈ 4 s behind aircraft; see above), (2) a "vertical wake-gap" which usually appears between the primary wake and the secondary wake after 50 s, (3) in part of the cases the primary wake disappears at the end of the vortex phase, while only the secondary wake becomes persistent.

Because of the uniform shape of the secondary wakes, when formed at all, we conjectured that detrainment due to one or more of the driving forces (i.e., baroclinic torque, shear, or turbulence) is always present at cruising conditions (disregarding the nonrealistic case of neutrally stratified atmosphere, zero shear, and zero turbulence, i.e., zero detrainment). The detrainment is a precondition for the formation of a visible secondary wake that seems to be always fulfilled. Therefore the observation that sometimes the detrained fluid becomes visible and sometimes not has to be controlled by a further parameter not addressed in this work. We postulate this is the level of ambient humidity. Consequently, in our subsequent paper we will combine lidar measurements and numerical simulations,

including microphysics, and treat ambient humidity as a free parameter. By this we will give an explanation for the vertical wake-gap and the disappearance of the primary wake at the end of the vortex regime. Ambient humidity is the key parameter for understanding the fact that sometimes a visible secondary wake is formed above the vortex pair and sometimes not [Sussmann and Gierens, this issue].

References

Antesberger, N., Beobachtung der thermodynamischen und geometrischen Eigenschaften von Kondensstreifen, diploma thesis, Fachhochsch. Munchen, Germany, 1996.

Bögel, W., and R. Baumann, Test and calibration of the DLR Falcon wind measuring system by maneuvers, J. Atmos. Oceanic Technol., 8, 5–18, 1991.

Chevalier, H., Flight test studies of the formation and dissipation of trailing vortices, J Aircraft, 10, 14–18, 1973.

Crow, S. C., Stability theory for a pair of trailing vortices, AIAA J., 8, 2172–2179, 1970.

Crow, S. C., and E. R. Bate Jr., Life span of trailing vortices in a turbulent atmosphere, J. Aircraft, 13, 476–482, 1976.

Danilin, M. Y., B. C. Krüger, and A. Ebel, Short-term atmospheric effects of high-altitude emissions, Ann. Geophys., 10, 904–911, 1992.

Durbeck, T., and T. Gerz, The dispersion of aircraft exhausts in the free atmosphere, J. Geophys. Res., 101, 26,007–26,015, 1996.

Ebert, E. E., and J. A. Curry, A parameterization of ice cloud optical properties for climate models, J. Geophys. Res., 97, 3831–3836, 1992.

Freudenthaler, V., F. Homburg, and H. Jäger, Contrail observations by ground-based scanning lidar: Cross-sectional growth, Geophys. Res. Lett., 22, 3501–3504, 1995.

Gerz, T., and T. Ehret, Wake dynamics and exhaust distribution behind cruising aircraft, in The Characterization and Modification of Wakes From Lifting Vehicles in Fluids, AGARD Conf. Proc., 584, 35.1–35.8, 1996.

Gerz, T., and T. Ehret, Wingtip vortices and exhaust jets during the jet regime of aircraft wakes, Aerosp. Sci. Technol., 7, 463–474, 1997.

Gerz, T., and B. Kärcher, Dilution of aircraft exhaust and entrainment rates for trajectory box models, in Proceedings on Impact of Aircraft Emissions Upon the Atmosphere, edited by J. Carpentier, vol. 1, pp. 271–276, Com. Avion Ozone, Onera, Paris, 1996.

Gierens, K. M., Numerical simulations of persistent contrails, J. Atmos. Sci., 53, 3333–3348, 1996.

Gierens, K. M., and J. Strom, A numerical study of aircraft wake induced ice cloud formation, J. Atmos. Sci., 55, 3253–3263, 1998.

Greene, G. C., An approximate model of vortex decay in the atmosphere, J. Aircraft, 23, 566–573, 1986.

Hauf, T., Aircraft observation of convection waves over Southern Germany—A case study, Mon. Weather Rev., 121, 3282–3290, 1993.

Hoshizaki, H., L. B. Anderson, R. J. Conti, N. Farlow, J. W. Meyer, T. Overcamp, K. O. Redler, and V. Watson, Aircraft wake microscale phenomena, in The Stratosphere Perturbed by Propulsion Effluents, CIAP, DOT-TST-75-53, chap. 2, Natl. Tech. Inf. Serv., Springfield, Va., 1975.

Jackson, P., K. Munson, L. Peacock, and J. W. R. Taylor (Eds.), Jane's All the World's Aircraft 1997-98, Jane's Inf. Group, Coulsdon, England, 1997.

Karcher, B., M. M. Hirschberg, and P. Fabian, Small-scale evolution of aircraft exhaust species at cruising altitudes, *J. Geophys. Res., 101*, 15,169–15,190, 1996a.

Karcher, B., T. Gerz, M. M. Hirschberg, and P. Fabian, Buildup of aerosol precursor gases and sulfur-induced activation of soot in nascent jet aircraft exhaust plumes, in *Impact of Aircraft Emissions Upon the Atmosphere*, edited by J. Carpentier, vol. II, pp. 503–508, Com. Avion Ozone, Onera, Paris, 1996b.

Karol, I. L., and Y. E. Ozolin, Small- and medium-scale effects of high-flying aircraft exhausts on the atmospheric composition, *Ann. Geophys., 12*, 979–985, 1994.

Lewellen, D. C., and W. S. Lewellen, Large-eddy simulations of the vortex-pair break-up in aircraft wakes, *AIAA J., 34*, 2337–2345, 1996.

Miake-Lye, R. C., M. Martinez-Sanchez, R. C. Brown, and C. E. Kolb, Plume and wake dynamics, mixing, and chemistry behind a high-speed civil transport aircraft, *J. Aircraft, 30*, 467–479, 1993.

Mishchenko, M. I., and L. D. Travis, Light scattering by polydispersions of randomly oriented spheroids with sizes comparable to wavelengths of observation, *Appl. Opt., 33*, 7206–7225, 1994.

Palikonda, R., P. Minnis, L. Nguyen, D. P. Garber, W. L. Smith Jr., and D. F. Young, Remote sensing of contrails and aircraft altered cirrus clouds, in *Impact of Aircraft Emissions Upon the Atmosphere*, edited by J. Carpentier, vol. II, pp. 439–444, Com. Avion Ozone, Onera, Paris, 1996.

Pasquill, F., and F. B. Smith, *Atmospheric Diffusion*, 3rd ed., Harwood, New York, 1983.

Quackenbush, T. R., M. E. Teske, and A. J. Bilanin, Dynamics of exhaust plume entrainment in aircraft vortex wakes, *AIAA J., 96-0747*, 16, 1996.

Robins, R. E., and D. P. Delisi, Numerical study of vertical shear and stratification effects on the evolution of a vortex pair, *AIAA J., 28*, 661–669, 1989.

Ruppersberg, G. H., and W. Renger, Invertierung der Lidarsignale von Cirrus und Kondensstreifen unter Nutzung des Schattenwurfes, *DLR-Forschungsber., 91-07*, Dtsch. Zent. für Luft- und Raumfahrt, Munich, Germany, 1991.

Saddoughi, S. G., and S. V. Veeravalli, Local isotropy in turbulent boundary layers at high Reynolds numbers, *J. Fluid Mech., 268*, 333–372, 1994.

Sarpkaya, T., and J. J. Daly, Effect of ambient turbulence on trailing vortices, *J. Aircraft, 24*, 399–404, 1987.

Sassen, K., The polarization lidar technique for cloud research: A review and current assessment, *Bull. Am. Meteorol. Soc., 72*, 1848–1866, 1991.

Schilling, V., S. Siano, and D. Etling, Dispersion of aircraft emissions due to wake vortices in stratified shear flows: A two-dimensional numerical study, *J. Geophys. Res., 101*, 20,965–20,974, 1996.

Schumann, U., On the effect of emissions from aircraft engines on the state of the atmosphere, *Ann. Geophys., 12*, 365–384, 1994.

Schumann, U., P. Konopka, R. Baumann, R. Busen, T. Gerz, H. Schlager, P. Schulte, and H. Volkert, Estimate of diffusion parameters of aircraft exhaust plumes near the tropopause from nitric oxide and turbulence measurements, *J. Geophys. Res., 100*, 14,147–14,162, 1995.

Scorer, R. S., and L. J. Davenport, Contrails and aircraft downwash, *J. Fluid Mech., 43*, 451–464, 1970.

Spalart, P. R., On the motion of laminar wing wakes in a stratified fluid, *J. Fluid. Mech., 327*, 139–160, 1997.

Spalart, P. R., and A. A. Wray, Initiation of the crow instability by atmospheric turbulence, in *The Characterisation and Modification of Wakes From Lifting Vehicles in Fluids, AGARD Conf. Proc., 584*, pap. 18, 1996.

Stockwell, W. R., Effects of turbulence on gas-phase atmospheric chemistry: Calculation of the relationship between timescales for diffusion and chemical reaction, *Meteorol. Atmos. Phys., 57*, 159–171, 1995.

Sussmann, R., Optical properties of contrail-induced cirrus: Discussion of unusual halo phenomena, *Appl. Opt., 36*, 4195–4201, 1997.

Sussmann, R., and K. M. Gierens, Lidar and numerical studies on the different evolution of vortex pair and secondary wake in young contrails, *J. Geophys. Res.*, this issue.

Sussmann, R., F. Homburg, V. Freudenthaler, and H. Jäger, Extrapolation of contrail investigations by lidar to larger scale measurements: Analysis and calibration of CCD camera and satellite images, in *Impact of Aircraft Emissions Upon the Atmosphere*, edited by J. Carpentier, vol. II, pp. 433–438, Com. Avion Ozone, Onera, Paris, 1996.

Tank, W., A climatology of lower stratosphere clear air turbulence, in *Proceedings of the 32nd Meeting on Aerospace Sciences, AIAA, 94-0377*, p. 18, Am. Inst. of Aeronaut and Astronaut., New York, 1994.

R. Sussman, Fraunhofer-Institut für Atmosphärische Umweltforschung, IFU, Kreuzeckbahnstrasse 19, D-82467 Garmisch-Partenkirchen, Germany. (sussmann@ifu.fhg.de)